PCCP

Accepted Manuscript

ROYAL SOCIETY OF CHEMISTRY

www.rsc.org/pccp

PCCP

ARTICLE

Onset potential behavior in α-Fe_2O_3 photoanodes: The influence of surface and diffusion Sn doping on the surface states†

Received 00th January 20xx,
Accepted 00th January 20xx

DOI: 10.1039/x0xx00000x

www.rsc.org/

Pravin S. Shinde,[a] Sun Hee Choi,[b] Yong Sam Kim,[b] Jungho Ryu,*[c] and Jum Suk Jang *[a]

The onset potential is an important parameter that affects the water oxidation performance of photoanodes. Herein, we investigate the behavior of the photocurrent onset potential of hematite (α-Fe_2O_3) photoanodes by incorporating Sn^{4+} cations via external (surface overlayer) or self (underlying FTO substrate) doping. The α-Fe_2O_3/FTO photoanodes fabricated at both low (550 °C) and high (800 °C) temperatures were chosen for surface Sn^{4+} doping (0–10 mM $SnCl_4$). At low temperature, the Sn^{4+} doping enriched the conductivity of α-Fe_2O_3/FTO, thereby improving the photocurrent response at higher applied potentials. In addition, the surface incorporation of Sn^{4+} shifted the onset of the water oxidation reaction in the positive direction. In the case of high temperature-annealed photoanodes, Sn leaching (resulting from FTO deformation) also affected the water oxidation performance of the photoanodes. This was caused by the loss in FTO conductivity as well as by the unfavourable surface properties due to the excess incorporation of Sn ions (SnO_x) into the hematite matrix. The anodic shift of the onset potential in both cases was due to the decreased surface state capacitance, as revealed by electrochemical impedance spectroscopy (EIS). The different annealing conditions, where lattice distortion and deformation-directed Sn diffusion-doping occur, were also found to affect the surface states associated with hematite and its water oxidation onset potential. Crystallographic analyses made via synchrotron XRD further support the results obtained from the EIS study. Sn doping was found to be concurrent with the respective changes in the (104) and (110) planes of hematite, which are associated with the onset potential-driving surface states and the photocurrent-boosting electron mobility, respectively.

Introduction

Hematite (α-Fe_2O_3) has sustained utilization in photocatalytic water splitting on account of its highest theoretical conversion efficiency (12.9%) promise among all the metal oxide semiconductors.[1] Additionally, it has a suitable band gap (E_g = 2.1 eV) in the visible light region and good electrochemical stability. However, despite its high theoretical efficiency, hematite suffers from inherent disadvantages such as a short hole diffusion length (~10 nm), poor oxygen evolution reaction kinetics, and high recombination rates. Recently, Sn doping has been shown to improve the photoelectrochemical water oxidation performance of hematite. This is achieved either by surface treatment or/and self-Sn diffusion doping from the underlying FTO (F:SnO_2) substrate. Unintentional Sn doping via high-temperature annealing has been effectively exploited to increase the electron donor density in order to enhance the photocurrent.[2-5] Moreover, surface treatment by various metal ions along with or without Sn ions has been used as a facile and effective way to improve the photocurrent performance of Fe_2O_3 photoanodes.[6-14] Despite of several surface treatment and doping studies, the influence of Sn on anodic or cathodic shifts in the onset potential is still unclear.[10] The purpose of these surface treatments is reportedly to suppress the number of defect states, which not only facilitates interfacial charge transfer but also controls the onset potential.

Recently, the role of surface states has garnered much interest, and a few studies revealed a strong correlation between the photocurrent onset potential and the surface states.[8, 9, 14-16] Surface states (also called interfacial states) are two-dimensional localized levels associated with the Fe_2O_3 surface that are caused by either oxygen vacancies (due to adsorbed ions) or crystalline disorder (due to abrupt distortion of the crystal lattice).[8, 17] It has also been suggested that these surface states sometimes play dual roles. In some cases, surface states are held responsible for the recombination of photogenerated electron-holes before taking part in the water oxidation reaction. In addition, they can also perform transit shipment of photogenerated holes and assist in speeding up the water oxidation reaction. Recently, Sivula *et al*. reported the state-of-the-art surface treatment approaches that reviews the surface modifications of various oxide and

---

[a] *Division of Biotechnology, Advanced Institute of Environmental and Bioscience, College of Environmental and Bioresource Sciences, Chonbuk National University, Iksan 570–752, Republic of Korea. E-mail: jangjs75@jbnu.ac.kr.*
[b] *Pohang Accelerator Laboratory (PAL), Pohang University of Science and Technology (POSTECH), Pohang 790–784, Republic of Korea.*
[c] *Mineral Resources Research Division, Korea Institute of Geoscience and Mineral Resources (KIGAM), Daejeon 305-350, Republic of Korea. E-mail: jryu@kigam.re.kr*

† Electronic Supplementary Information (ESI) available: Table S1–S3, Synchrotron XRD, FESEM, survey XPS spectra, EXAFS, and UV–vis spectroscopy. See DOI: 10.1039/x0xx00000x

chalcogenide semiconductor materials for improving the light harvesting efficiency.[18]

In general, the enhanced performance of hematite, due to various surface treatments such as SnO_2,[7] Al_2O_3,[8, 11] Ga_2O_3,[19] TiO_2,[8, 12, 20] ZnO,[13] SiO_x,[21] etc.), has been attributed to the passivation or reduction of surface states. Surface incorporation of Al^{3+} and Sn^{4+} ions at 520 °C resulted in the formation of Fe_2O_3–Al_2O_3 or Fe_2O_3–SnO_2 solid solution coatings on the Fe_2O_3 surface. These coatings reduced the surface states and/or the back reactions that were caused by electrons leaking at the α-Fe_2O_3/electrolyte interface and improved the photo-response of α-Fe_2O_3 films with a cathodic shift of ~100 mV.[7] Sn-decoration of flame-annealed hematite nanoflakes exhibited higher photocurrent at the cost of anodic shift in the onset potential. On the hand, addition of Sn showed positive effect by shifting the onset potential in cathodic direction, but resulted in with lower photocurrent performance. A 100–200 mV cathodic shift in the onset potential was observed when α-Fe_2O_3 was treated with a thin overlayer of Al_2O_3 or Ga_2O_3.[8, 11, 19] A 170 mV cathodic shift in the onset potential, caused by three cycles of a zinc acetate surface treatment, was ascribed to a ZnO overlayer that changes the flat band potential of hematite and reduces the surface defects.[13] The extent of surface treatment also determines the progress of water oxidation photocurrent and the onset potential. For example, an ultra-thin TiO_2 layer, which create a sufficient amount of defect states without blocking the hole transfer, can enhance the photocurrent of hematite with cathodic shift in onset potential, however a too thick layer can block the hole transfer leading to anodic shift in the onset potential.[12]

In a different approach, Bisquert and co-workers suggested a surface trap-mediated charge transfer process at the hematite-electrolyte interface to explain the shift in onset potential based on a comprehensive electrochemical impedance spectroscopy (EIS) technique. According to their study, water oxidation takes place predominantly from surface trapped holes and not directly from valence band holes.[15] In this type of charge transfer mode, the surface states help charge injection at the hematite and electrolyte interface. These surface trap states provide the primary pathways of charge transfer at the surface through resonance tunneling.[22] In such cases, the hole accumulation has been characterized by several advanced electrochemical methods via direct and indirect measurement of the surface state capacitance with (photo)electrochemical impedance spectroscopy (EIS or PEIS).[15, 23-25] Dunn et al. with the help of intensity-modulated photocurrent spectroscopy (IMPS) elucidated that Sn-doping speeds up light-driven water oxidation on hematite by increasing the rate constant for hole transfer by almost ten-fold degree.[26]

From above-mentioned studies, it is clear that the Sn doping and surface modifications need to be performed carefully as these can positively or negatively affect the photocurrent onset potential, which in turn decides the water oxidation reaction to be faster or sluggish, respectively. Thus onset potential remains an important factor to be investigated. However, despite the promising results enabled by Sn doping and surface treatments in enhancing photocurrent response, a systematic study with regard to Sn doping/surface modification and the resulting onset potential behavior of Sn-doped α-Fe_2O_3 photoanodes has not yet been explored.

In this study, we investigate the effect of Sn^{4+} doping on the surface and crystalline properties of planar hematite photoanodes that are fabricated by the pulse reverse electrodeposition (PRED) method and also analyse the resulting photocurrent performance of these photoanodes. The main objective is to study the impact of Sn doping (surface treatments of different Sn ion concentrations) and different annealing temperatures and methods (self Sn diffusion doping from the deformation of FTO at high temperature) on the photocurrent onset potential behavior of Sn-doped α-Fe_2O_3 photoanodes. A powerful EIS tool was used to account for the hole transport phenomena in hematite and to determine the origin of the shift in the onset potential caused by Sn incorporation.

Experimental details

Synthesis of pristine and Sn-doped α-Fe_2O_3 photoanodes

Iron films were grown on fluorine-doped tin oxide (FTO, F:SnO_2, 10–15 sq. cm^{-1})-coated glass substrates by a PRED method. The cleaning procedure used for the FTO substrates and the synthesis parameters of PRED, including the amplitude of the square wave pulse (10 V [–6/+4 V]), duty cycle (20%), pulse period (10 ms), and deposition time (45 s), were chosen according to a previous study.[27] The chemicals were purchased from Alfa Aesar and Kanto Chemical Co. and were used as-received.

To investigate the correlation between surface-treated Sn ion concentration on the onset potential and photocurrent performance of hematite films (Fe_2O_3/FTO), the as-grown iron (Fe/FTO) electrodes were annealed at low temperature (LT). The surface Sn^{4+}-loading was accomplished by dipping the as-grown Fe/FTO electrodes into different concentrations of $SnCl_4$ solutions (viz. 0, 1, 5, and 10 mM) for 2 min, drying with a slow stream of nitrogen, annealing at 550 °C for 4 h, and then cooling down to ambient temperature naturally. The corresponding photoanodes were designated as LT550, LT550-Sn1, LT550-Sn5, and LT550-Sn10, respectively.

In the second step, different types of Fe_2O_3/FTO photoanodes were prepared at high temperature (HT) to determine the effect of self-Sn-doping and FTO deformation during HT-annealing. The Fe_2O_3/FTO photoanodes, which were fabricated from the as-grown Fe/FTO electrodes by a one-step annealing process[2] at 800 °C and 825 °C for 13.5 min, were designated as D800 and D825, respectively. The Fe_2O_3/FTO photoanode fabricated via a two-step annealing method, using the LT-annealed photoanode at 800 °C for 13.5 min, was designated as STP800. In the third step, the effect of Sn^{4+} (from the surface treatment) and Sn (from FTO deformation) on the onset potential behavior of hematite fabricated by the two-step and one-step methods was investigated. The Sn-doped hematite photoanode by two-step method (designated as

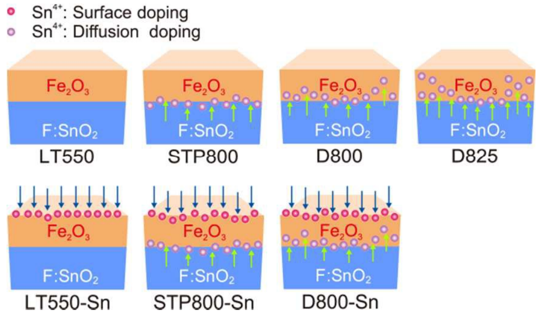

Scheme 1. Schematic showing formation of α-Fe_2O_3 films with two different Sn^{4+} doping strategies (surface and diffusion doping) using different annealing approaches.

STP800-Sn1) was fabricated first by LT-annealing of the as-grown Fe/FTO at 550 °C for 4 h, followed by surface treatment with 1 mM Sn^{4+} and subsequent HT-annealing at 800 °C for 13.5 min. Sn-doped hematite made by the one-step method (designated as D800-Sn1) was prepared by treating the surface of as-grown Fe/FTO with 1 mM Sn and then HT-annealing at 800 °C for 13.5 min. The Sn concentration for D800 samples was further increased to 5 and 10 mM; these samples were designated as D800-Sn5 and D800-Sn10, respectively. Scheme 1 shows the fabrication of pristine and Sn-doped Fe_2O_3 photoanodes via different annealing approaches using Sn^{4+} surface and diffusion doping strategies.

Material characterization

The structural characterizations of representative pristine and Sn-doped Fe_2O_3 samples were performed using synchrotron X-ray diffraction (XRD). Synchrotron XRD measurements were carried out with an incident X-ray energy of 8.9 keV (equivalent to an X-ray wavelength of 0.1393 nm) at the 9C beamline at the Pohang Light Source II in Korea. The obtained data was normalized by the ionization chamber by monitoring the incident X-ray beam intensity. The refinement of XRD patterns was carried out to determine the lattice parameters.

The morphologies of the pristine and Fe_2O_3 films were determined using a field-emission scanning electron microscope (FESEM) (SUPRA 40VP, Carl Zeiss, Germany) that was equipped with an X-ray energy dispersive spectrometer (EDS). The hematite samples were sputter-coated with osmium before FESEM examination.

The chemical state and elemental quantification in the freshly-synthesized iron oxide samples was performed using X-ray photoelectron spectroscopy (XPS). XPS measurements were carried out using a PHI Quantera II instrument equipped with a monochromatic Al Kα X-ray source (hν = 1486.6 eV, 40 W, and 15 kV). The detection angle relative to the substrate surface was 45°. The wide survey spectra (binding energy, BE: 1200−0 eV) were recorded for the samples using an X-ray spot size of 200 µm at room temperature with an analyzer pass energy of 280 eV and an energy step size of 1 eV. High resolution spectra in the region of interest were acquired at a pass energy of 55 eV and a step size of 0.1 eV. The calibration of the binding energy of the high resolution spectra of all of the iron oxide samples was made by referencing the maximum of the adventitious C 1s peak at 284.8 eV. XPS data was processed with the help of an XPS peak-fit program.

To observe the Sn doping across representative Fe_2O_3/FTO photoanodes, full cross-sectional TEM samples were prepared with a dual-beam focused ion beam (FIB) (Helios NanoLab, FEI) using a Ga^+ ion beam source operated at 30 kV. The elemental analysis and elemental line profile mapping across the cross-section were performed with a field-emission transmission electron microscope (JEM-2100F HR, JEOL) operated at 200 kV. This was equipped with an energy dispersive spectrometer (EDS).

The local structures of the pristine and Sn-doped iron oxide electrodes were investigated with X-ray absorption fine structure (XAFS). Extended X-ray absorption fine structure (EXAFS) experiments were performed on the 7D beamline of the Pohang Accelerator Laboratory (PLS-II, 3.0 GeV, 400 mA). The synchrotron radiation was monochromatized using a Si(111) double crystal monochromator. At room temperature, the spectra for the Fe K-edge (E_0=7112 eV) were taken in a fluorescence mode. The incident beam was detuned by 30% for the Fe K-edge in order to minimize contamination from higher harmonics, and its intensity was monitored using a N2-filled IC SPEC ionization chamber. The fluorescence signal from the sample was measured with a PIPS (passivated implanted planar silicon) detector. During the measurements, helium was continuously surged into the chamber containing the sample so that the air-scattering of the fluorescence signal was minimized to obtain a spectrum with a higher S/N ratio. The energy was scanned with 5 eV steps between 6912 and 7062 eV, 1 eV steps between 7062 and 7102 eV, 0.3 eV steps between 7102 and 7152, 1.7 eV steps between 7152 and 7660 eV, and 4.1 eV steps between 7660 and 7969 eV for 2, 2, 2, 3, and 3 s per point for integration, respectively. ATHENA, from the IFEFFIT suite of programs, was used to analyse the obtained data for the local structure study of Fe in α-Fe_2O_3 photoanodes.[28] A standard for fitting the experimentally-derived Fourier-transformed spectra was generated with FEFF9 code[29] using a known α-Fe_2O_3 structure.[30]

The UV-Vis absorption study in the wavelength range between 350 and 800 nm was performed using a dual beam spectrophotometer (Shimadzu, UV-2600 series).

Photoelectrochemical (PEC) measurements

The PEC experiments were performed in a typical PEC cell consisting of a three-arm glass compartment equipped with a quartz window for frontal illumination.[31] All the tests were carried out in a three-electrode configuration using the pristine or Sn-doped Fe_2O_3/FTO photoanode as working electrode for the water photo-oxidation reaction, a platinum coil as the counter electrode, and an Ag/AgCl (saturated with KCl) as the reference electrode, immersed in an aqueous 1 M NaOH electrolyte. A simulated 1 sun (100 mW cm^{-2}) light illumination was provided from front-side using a solar simulator (Abet Technologies). The photocurrent density–voltage (*J*–*V*) curves, electrochemical impedance spectroscopy (EIS), and Mott–Schottky studies were performed using a portable potentiostat (COMPACTSTAT.e, Ivium, Netherlands) equipped with an electrochemical interface and an impedance analyzer. Only 1 × 1 cm^2 area of photoanode under investigation was immersed and exposed to light by covering the rest with a Teflon tape. The reproducibility of the measured data was verified by repeating the PEC measurement of the photoanodes prepared under identical conditions on at least three different days. All the potentials mentioned in this work were originally measured with reference to Ag/AgCl electrode (*sat*. KCl) and were converted to the reversible hydrogen electrode (RHE) scale using the Nernst equation (1).[32]

$$E_{\mathrm{RHE}} = E_{\mathrm{Ag/AgCl}} + 0.059 \cdot \mathrm{pH} + E^{\mathrm{o}}_{\mathrm{Ag/AgCl}} \qquad (1)$$

where E_{RHE} is the revised potential vs. RHE in V vs. RHE (V_{RHE}), $E_{\mathrm{Ag/AgCl}}$ is the experimental potential measured against the Ag/AgCl reference electrode in V vs. Ag/AgCl ($V_{\mathrm{Ag/AgCl}}$), and $E^{\mathrm{o}}_{\mathrm{Ag/AgCl}}$ is the standard potential of Ag/AgCl (*sat*. KCl) at 25 °C (i.e. 0.1976 V).

EIS curves were recorded from 0.1 Hz to 100 kHz, with AC amplitude of 10 mV, at the water splitting potential (at 1.23 V_{RHE}) under simulated 1 sun illumination. The experimental EIS data were validated using the Kramers–Kronig transform test and then fitted to suitable equivalent circuit models using the ZView (Scribner Associates Inc.) program, which is based on the nonlinear least-squares Levenberg-Marquardt algorithm. Fitting of the measured EIS data was achieved using appropriate electrochemical circuits.

Mott–Schottky measurements were performed in a dark condition with a DC applied potential window of -0.6 to 0.7 V *vs*. Ag/AgCl at an AC frequency of 0.5 kHz and a scan step of 0.05 V. The amplitude of the AC voltage was 10 mV. The electron donor densities were estimated from the slopes of the Mott–Schottky plot (C_{sc}^{-2} *vs*. V) using the equation for planar electrodes:[33]

$$N_{\mathrm{D}} = (2/\mathrm{e}\varepsilon\varepsilon_{\mathrm{o}})[\mathrm{d}(C_{\mathrm{sc}}^{-2})/dV]^{-1} \qquad (2)$$

where C_{sc} is the space charge layer capacitance, e is the electron charge (1.6022 × 10^{-19} C), ε is the dielectric constant of α-Fe_2O_3 (80),[34] ε_{o} is the permittivity of a vacuum (8.854 × 10^{-14} F cm^{-1}), N_{D} is the donor density, and V is the applied potential.

Results and discussion

X-ray diffraction (XRD)

Fig.S1a (ESI†) shows the synchrotron XRD patterns recorded in the diffraction angle (2θ) range between 20 and 70°, of LT550 and LT550-Sn10 photoanodes. It is obvious that surface treatment with Sn^{4+} lowered the hematite peak intensities without noticeably shifting the peak positions, which is an indication of suppressed hematite crystallinity. This suggests that Sn^{4+} surface treatment before LT-annealing at 550 °C inhibits hematite growth and affects the surface properties. Fig.S1b (ESI†) shows the XRD patterns of pristine α-Fe_2O_3 photoanodes (LT550, STP800, D800, and D825) fabricated under different annealing conditions without Sn^{4+} surface treatment. Among the various planes, the major (104) and (110) planes of α-Fe_2O_3 are of particular interest in this study.

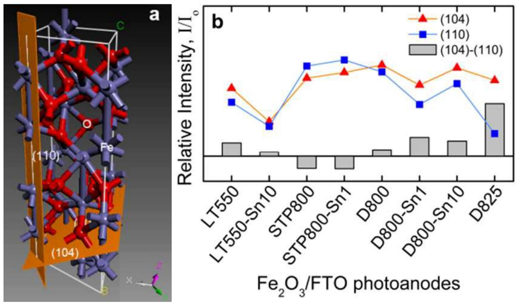

Fig. 1 (a) Hematite surface orientation of (104) and (110) planes and (b) plot of relative intensities of major hematite peaks, such as (104) and (110), for pristine and Sn-doped α-Fe_2O_3 photoanodes fabricated with different annealing conditions.

The relative intensity of the major (104) peak is highest for D800 and is decreased for other samples in the order of STP800 > D825 > LT550 (See Table S1, ESI†). The position of the SnO_2 peaks (from FTO substrate) shifted slightly toward a smaller diffraction angle, by a margin of 0.04° from LT550 to D825. The shift in the substrate peak positions is variable, suggesting the existence of a disordered or distorted SnO_2 lattice (as a result of different annealing conditions). However, this observation requires further analysis. Fig.S1c (ESI†) shows the XRD patterns of the pristine and 1 mM Sn-doped α-Fe_2O_3 photoanodes fabricated at 800 °C by the two-step and one-step annealing methods. The hematite peak intensities in STP800 are slightly higher than those in D800, which was further enhanced by 1 mM Sn^{4+} surface doping. Alternatively, the substrate peak intensity is lower for STP800 in comparison with D800. The substrate peaks exhibited a shift toward lower angles, suggesting that the Sn^{4+} doping caused the hematite lattice to expand. Lattice expansion due to Sn^{4+} doping can be witnessed from the increased hematite volume, as shown in Table S2 (ESI†). The addition of 1 mM Sn^{4+} caused an increase and a decrease in the intensities for the STP800 and D800 samples, respectively. Fig.S1d (ESI†) shows the XRD patterns of pristine and Sn-doped α-Fe_2O_3 photoanodes fabricated by the one-step HT-annealing method with surface treatments of 1 and 10 mM Sn^{4+}. The Sn-doped hematite showed a decrease in peak intensity as the surface Sn^{4+} ion concentration is increased from 0 to 10 mM. The substrate peak positions were also shifted to lower angles upon the addition of Sn ions, clearly indicating lattice expansion (as seen from the volume increase displayed in Table S2, ESI†). Here, incorporation of Sn^{4+} into hematite comes from two sources: from the external surface treatment and from Sn diffusion due to FTO deformation. Additionally, the deformation behavior of FTO (or SnO_2) alone, under different annealing conditions, was carried out. Fig.S1e (ESI†) shows the XRD patterns of as-cleaned bare and annealed FTO electrodes fabricated at different annealing conditions. The stoichiometric cassiterite tetragonal structure of SnO_2 (PDF#01-077-0452, space group: P42/mmm(136), a=b=4.7552 Å, c=3.1992 Å) was retained for bare FTO, although the high index planes deviate from the standard diffraction data. The SnO_2 peak positions were shifted toward lower 2θ angles, suggesting lattice expansion.

More severe distortion in the SnO_2 lattice was observed for one-step annealed FTO (825 °C for 13.5 min).

The polycrystalline α-Fe_2O_3 layers are generally randomly oriented in directions such as [110], [104], [300], [012], and [024]. The surface that is oriented in the [110] preferential direction is dominated by Fe(III) stoichiometric termination; whereas the surface oriented in the [104] direction is predominantly composed of surface-terminated O_2^- groups. Fig.1a shows the hematite surfaces oriented in the (104) and (110) directions. It was reported that oxygen vacancies act as electron traps or surface defects.[35] The probability of defect states is expected to be much higher for the (104) plane since it has a greater proportion of terminal oxygen ions.[36] The electron and hole mobilities are also lower within the (104) plane. Hence, the (110) plane is believed to be more conducting than the (104) plane. The various preferential orientations of hematite crystallites also determine the organization of the terminating atoms (Fe, O) at the surface, which eventually decide the degree of the surface states. Fig.1b shows the plot of relative intensities (I/I_o) of major hematite peaks, such as (104) and (110), for pristine and Sn-doped α-Fe_2O_3 photoanodes fabricated with different annealing conditions (see also Table S1, ESI†). Here, I is the intensity of the (*hkl*) peak and I_o is intensity of the most intense (*hkl*) peak in the XRD pattern (after background subtraction). It is interesting to note that the relative intensity from the (104) plane is higher than that of the (110) plane for LT550 and all of the one-step annealed D800 samples. Among the one-step annealed samples, the difference in the intensities between the (104) and (110) planes increases upon the addition of external Sn, with the (104) plane being predominant. In contrast, the intensity of the (104) plane decreases for the two-step annealed pristine and Sn-doped Fe_2O_3. Thus, the preferential growth of (104) is more favourable for one-step annealed Sn-doped Fe_2O_3.

Because Sn is diffusing from both the bottom and the top surface of Fe_2O_3 at high temperatures, it is important to consider changes in the lattice parameters. Table S2 (ESI†) shows the average lattice parameters of Fe_2O_3 (rhombohedral) and SnO_2 (tetragonal), as determined from the synchrotron XRD, for pristine and Sn-doped Fe_2O_3 photoanodes fabricated by different annealing temperatures and methods. The experimental lattice constants and c/a ratio of α-Fe_2O_3 are close to previous theoretical reports and standard values ($a = b = 5.039$ Å, $c = 13.770$ Å, $c/a = 2.733$).[37] The LT-annealed and two-step annealed α-Fe_2O_3/FTO samples exhibited a lattice volume of ~301 Å^3, which is increased slightly to ~302 Å^3 for the one-step annealed α-Fe_2O_3/FTO samples; this confirms that the lattice expansion may be due to the incorporation of excess Sn ions. In addition, it is interesting to note that the SnO_2 lattice in the one-step annealed α-Fe_2O_3/FTO increases upon the incorporation of Sn: the lattice volume increases from 72.77 to 73.04 Å^3. The lattice volume of SnO_2 in pristine α-Fe_2O_3/FTO annealed at 825 °C is similar to that of 10 mM Sn-doped α-Fe_2O_3/FTO, but the volume of the Fe_2O_3 lattice has not increased. Thus, annealing at 825 °C only brings about substrate deformation, which causes volume expansion.

Morphological study

Fig.S2a (ESI†) shows the FESEM images of pristine and Sn-doped α-Fe_2O_3 photoanodes fabricated at a low annealing temperature with different surface concentrations of Sn^{4+} (0 to 10 mM). The thickness of the hematite film is *ca*. 200 ±20 nm, as reported previously.[27] The surface of pristine α-Fe_2O_3 shows a nanostructured morphology that consists of compactly packed nano-crystalline grains with good particle inter-connectivity. Although the grain size varies from 20 to 60 nm, the distribution of the smaller grains is higher. Additionally, nano-rods up to 400-500 nm in length and 40 nm in diameter also appear. The surface treatment with 1 mM Sn^{4+} before LT-annealing results in grain growth as well as a reduction in the nano-rod overgrowths. With further increases in the Sn^{4+} concentration up to 5 and 10 mM, grain growth occurs with disappearance of nano-rods from the surface leading to a decrease in the surface roughness. Such microstructure modification can be attributed to the fact that the adsorption of Sn^{4+} ions on the surface before LT-annealing leads to segregation, consequently decreasing the surface energy. Fig.S2b (ESI†) shows the FESEM images of pristine α-Fe_2O_3 photoanodes prepared with different annealing conditions (LT550, STP800, D800, and D825). The morphology of STP800 reveals less inter-connectivity between the particles as compared to that of D800. The D825 sample exhibits larger grains with less inter-connectivity, as seen from the increased space between the grain boundaries. Fig.S2c (ESI†) shows the FESEM images of pristine and Sn-doped α-Fe_2O_3 photoanodes fabricated by the two-step and one-step HT-annealing methods. The addition of 1 mM Sn^{4+} during two-step-annealing of hematite resulted in a decrement of the nano-rod structures on the surface of Sn-doped α-Fe_2O_3 with a slight decrease in the grain size. However, Sn-doped α-Fe_2O_3 prepared by one-step-annealing with a similar Sn concentration demonstrated a significant improvement in the grain size. Hence, the Sn^{4+} concentration was further varied for one-step annealed hematite electrodes. Fig.S2d (ESI†) shows the FESEM images of pristine and Sn-doped α-Fe_2O_3 photoanodes fabricated by the one-step annealing method at 800 °C. Grain growth is apparent for Sn^{4+} concentrations up to 5 mM. The 5 mM Sn^{4+} in α-Fe_2O_3 instigates the cluster formation of smaller and larger grains. A greater amount of cluster formation and a decrease in the grain size is evident for Sn-doped α-Fe_2O_3 with 10 mM Sn^{4+}. This suggests that increasing the Sn content has a deleterious effect on the surface irregularities as well as on grain growth. Excess Sn, which is not doped into the lattice, may be converted into a resistant SnO_x layer on the α-Fe_2O_3 surface, blocking its interaction with its surroundings.

X-ray photoelectron spectroscopy (XPS)

The compositions of pristine and Sn^{4+} surface-treated Fe_2O_3 samples fabricated by different annealing methods were studied by XPS (See Fig.S3a–d, ESI†, for survey XPS spectra).

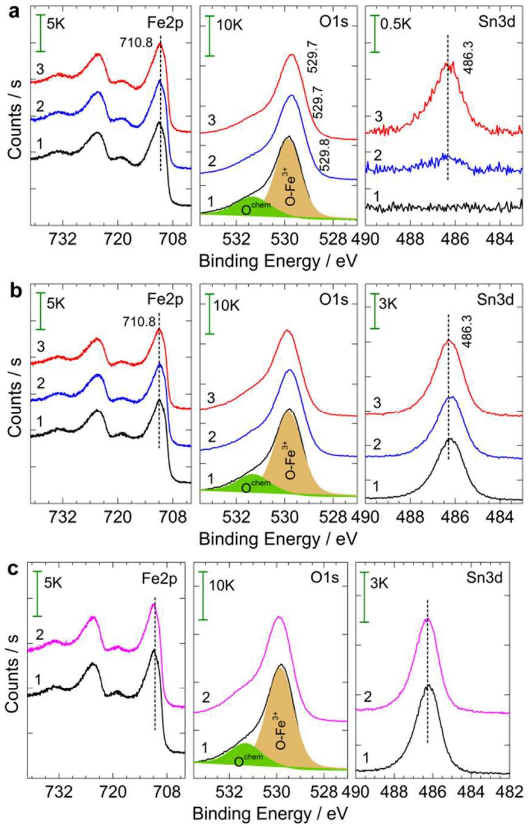

Fig. 2 High resolution XPS spectra for Fe2p, O1s, and Sn3d regions of pristine and Sn-doped α-Fe_2O_3 photoanodes fabricated by (a) LT-annealing (550 °C for 4 h) and one-step HT-annealing (800 °C for 13.5 min) with Sn concentrations of 1) 0 mM, 2) 5 mM, and 3) 10 mM; (c) Survey XPS spectra of un-treated α-Fe_2O_3 photoanodes fabricated by one-step HT-annealing at 800 °C and 825 °C for 13.5 min.

Table 1 The elemental ID and quantification of pristine and Sn-doped Fe_2O_3 films fabricated by LT (550 °C) and HT (800 °C and 825 °C) annealing treatments. Peak values were calibrated with reference to adventitious carbon at 284.8 eV.

Samples	Fe 2p		O 1s		Sn 3d5	
	BE	at. %	BE	at. %	BE	at. %
LT550	710.8	36.69	529.8	63.31	----	<0.1
LT550-Sn5	710.8	36.65	529.7	63.24	486.3	0.11
LT550-Sn10	710.8	36.56	529.7	63.09	486.3	0.35
D800	710.8	36.02	529.8	62.16	486.2	1.82
D800-Sn5	710.8	35.98	529.8	62.09	486.2	1.93
D800-Sn10	710.8	35.82	529.9	61.81	486.3	2.37
D825	710.8	35.94	529.9	62.02	486.3	2.04

Fig.2a shows the high resolution XPS spectra of the Fe 2p, O 1s, and Sn 3d5 elements for pristine and Sn-doped Fe_2O_3 photoanodes fabricated by LT-annealing (550 °C) with 5 and 10 mM Sn^{4+} surface treatments. Table 1 shows the elemental quantifications obtained from these peaks. In the Fe 2p region, an Fe $2p_{3/2}$ peak was observed at a binding energy (BE) of 710.8 ± 0.1 eV, suggesting that the oxidation state of Fe is +3. This confirms the formation of phase-pure α-Fe_2O_3.[38, 39] The lowest BE peak in O 1s (centered around 530 eV) was assigned to oxygen atoms in the iron oxide lattice (O 1s(Fe−O)), and the peak around 531 eV was assigned to the lattice hydroxyl groups (O 1s(Fe−OH lattice)).[38, 40] The O 1s(Fe−O) peak for the pristine sample is close to the ideal value (529.9 eV). However, a slight shift in its position toward a lower BE in the Sn-doped samples could be due to the slightly disordered electronic structure caused by the incorporation of Sn into Fe_2O_3. The shapes of the Fe 2p and O 1s spectra are similar to those reported for α-Fe_2O_3.[41] The pristine sample did not show the presence of the Sn $3d_{5/2}$ peak at 486.2 ± 0.3 eV. This suggests that Sn did not diffuse into the Fe_2O_3 from the FTO or the diffused percentage is negligibly small to be detectable by XPS. In the doped hematite, Sn was reported to exist in hematite with a 4+ oxidation state. However, the appearance of the Sn $3d_{5/2}$ peak at a slightly lower BE (486.2 eV) in the present study compared to that of SnO_2 (~486.3 ± 0.1 eV) could be related to the oxygen-deficient SnO_x phase. As the Sn content is increased, the BE value increased to 486.3 eV, indicating more oxide formation of Sn. Sn contents of *ca.* 0.1 and 0.3 at% were appeared for the 5 mM and 10 mM Sn-doped Fe_2O_3 samples (Table 1). Fig.2b shows the high resolution XPS spectra of pristine and Sn-doped α-Fe_2O_3 photoanodes fabricated by one-step HT-annealing (800 °C) with 5 and 10 mM Sn^{4+} surface treatments. The nature of spectra is similar, with the exception of a noticeable increase in the Sn 3d5 peak intensity. This suggests that, at elevated annealing temperatures, leaching and diffusion of Sn (from the underlying FTO substrate) into the Fe_2O_3 matrix occurs; this increases the Sn at% in the hematite lattice.

Such unintentional Sn doping in Fe_2O_3 is advantageous for improving the photocurrent response.[5] The Sn content in the pristine D800 sample was *ca.* 1.82 at%. Upon the addition of 5 and 10 mM Sn^{4+}, the total Sn concentration was increased to *ca.* 1.93 and 2.37 at%, respectively. Although a greater amount of Sn appeared in the 10 mM Sn-doped Fe_2O_3, the state of Sn in the lattice and the conductivity behavior of FTO determine the overall photo-response of the photoanodes. As can be seen, the BE value of Sn is slightly higher in the D800-Sn10 sample (486.3 eV) than it is in the D800 and D800-Sn5 samples. This means that the oxidized state of Sn (SnO_x formation) is higher in the former sample. The formation of a resistant SnO_x oxide layer can change the surface state properties of hematite and limit the charge transfer processes that occur at the electrolyte interface. Fig.2c shows the high resolution XPS spectra of D800 and D825 samples. D825 sample shows a higher Sn content of *ca.* 2.04 at% compared to D800 (*ca.* 1.82 at%). This suggests that more Sn is leeched from the FTO (forming resistive SnO_x) causing severe deformation. As a consequence, the conductivity of FTO is decreased. Optimum FTO conductivity is necessary for efficient collection of the majority charge carriers toward the back contact. Hence, it is imperative to maintain an appropriate balance among the amount of Sn leeched from FTO, the structural ordering of the hematite lattice, and a minimal loss in the FTO conductivity.

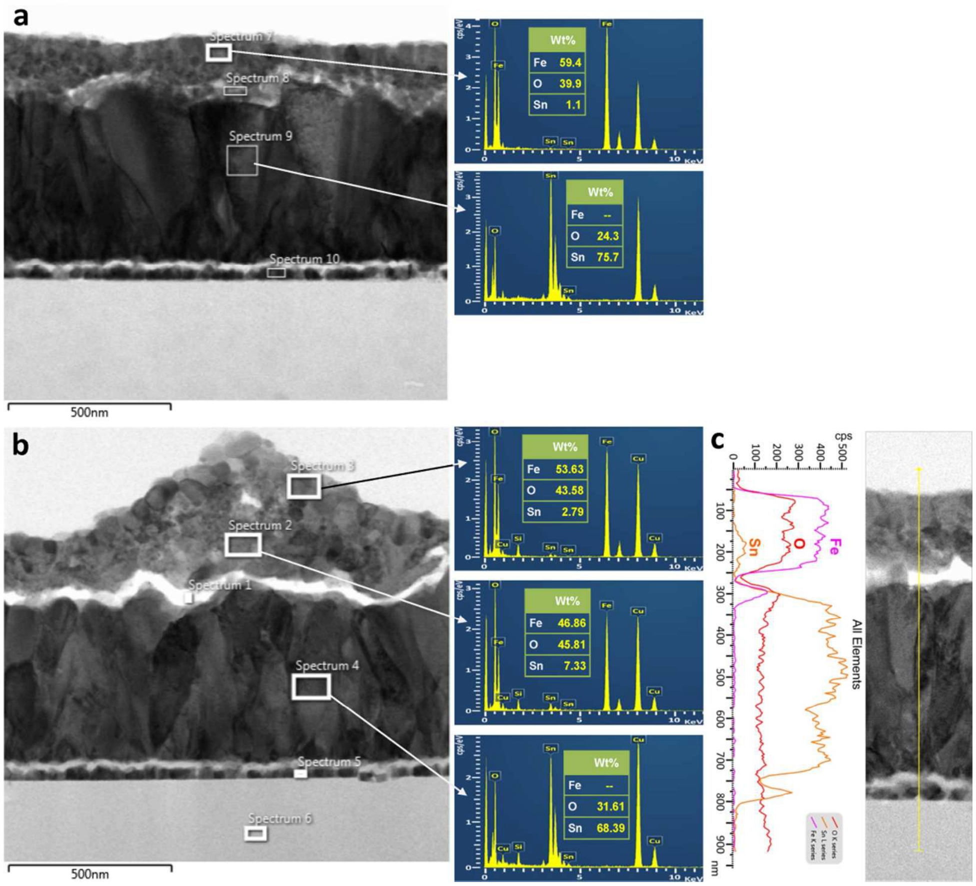

Fig. 3 Cross-sectional TEM micrographs after FIB cutting of the (a) LT550-Sn10 and (b) D800-Sn10 samples with their respective EDS spectra revealing the wt% compositions of Fe, O, and Sn elements. (c) Line profile obtained from TEM-EDS analysis for the D800-Sn10 sample, revealing the diffusion of Sn ions from FTO.

Cross-sectional TEM and EDS

To gain insights on the behavior of Sn doping resulting from both the surface and FTO deformation, cross-sectional TEM micrographs of the LT550 and D800 photoanodes (with a 10 mM Sn^{4+} ion surface treatment) were prepared using FIB. The point EDS spectra were recorded to determine the elemental composition at selective regions of the cross-section in order to reveal the concentration of Sn doped either via the surface treatment or from FTO. The surface treated LT550 shows 1.1 wt% Sn near the hematite surface. Considering the fact that FTO deformation does not occur at low temperatures, the amount of Sn in FTO remains unchanged (at 75.7 wt%), as shown in Fig.3a. In the case of the D800 sample (Fig.3b), the Sn content in FTO is reduced to 68.39 wt%. This is because in the deformed state at 800 °C, part of Sn^{4+} ions of FTO also diffuses into the hematite matrix, up to the hematite surface. The Sn content near the hematite surface is 2.79 wt%, which is higher than that of the LT550 sample. Also, the Sn content in the bulk hematite is around 7.33 wt%, which is the combined amount of surface Sn^{4+} and Sn-diffusion from FTO (with a higher contribution from the latter source). A TEM-EDS line profile (Fig.3c) obtained from the cross-section of the D800-Sn10 sample, reveals the diffusion of Sn into the hematite matrix.

X-ray absorption fine structure (XAFS)

To further elucidate the structural disordering in pristine and Sn-treated Fe_2O_3 photoanodes, X-ray absorption fine structure studies were performed. The extended X-ray absorption fine structure (EXAFS) is an element-specific and bulk local structure-determining probe. Fig.4a depicts the Fourier-transformed spectra of EXAFS functions for Fe K-edges of LT550 and LT550-Sn10 samples. Two distinct peaks appear within a radial distance of 4 Å: one at 0.8–2.1 Å and another at 2.1–3.9 Å. The former is due to the nearest Fe−O bonds and the latter is due to contributions from Fe−M (M=Fe or Sn) and Fe−O bonds at a longer distance. Both the LT550 and LT550-Sn10 samples exhibit higher peak intensities than that of the reference α-Fe_2O_3 powder sample, indicating increased bond orderings in the films on the FTO substrate. The peak at 0.8–2.1 Å for LT550-Sn10 exhibits a lower intensity and is shifted slightly to a higher distance when compared with LT550. This aforementioned observation is supported by the structural parameters that were obtained from the EXAFS fits shown in Table S3 (ESI†). Two Fe−O bond distances (R1 and R2) for LT550 were increased by 0.04 Å due to the Sn surface treatment. The Debye Waller factor, an indicator of the structural disorder, is much smaller for both the LT550 and

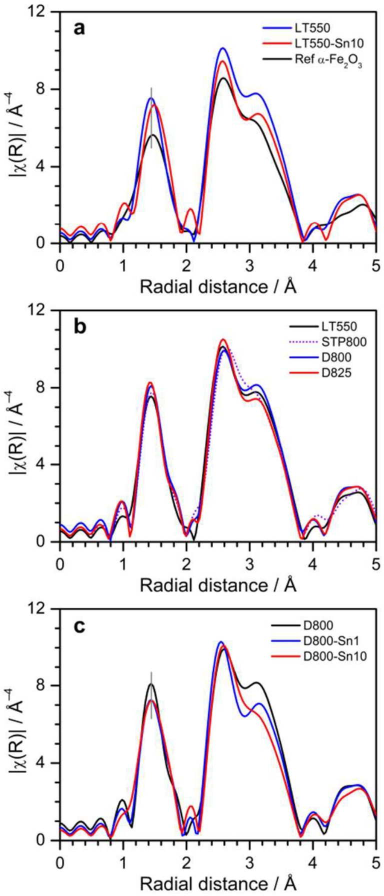

Fig. 4 The k^3-weighted Fourier transforms of EXAFS functions for Fe K-edges of (a) untreated and Sn-treated α-Fe_2O_3 photoanodes fabricated by LT-annealing at 550 °C, (b) α-Fe_2O_3 photoanodes fabricated at different annealing temperatures (550 °C, 800 °C, and 825 °C) and by different methods (STP800 and D800 / D825), and (c) untreated and Sn-treated α-Fe_2O_3 photoanodes fabricated by HT-annealing at 800 °C.

LT550-Sn10 samples than it is for the reference α-Fe_2O_3 powder sample. A minor increase in the Debye Waller factor is observed for LT550-Sn10 when compared with LT550. For the second peak (at 2.1–3.9 Å), which consists of several complicated scatterings, each shell cannot be separated and it is not discussed further in this paper. Fig.4b reveals the effects of annealing temperature and annealing method on the structural ordering of photoanodes. The intensity of the peak at 0.8–2.1 Å increases in the order of LT550~STP800 < D800~D825. While the EXAFS function is generally k^3-weighted before the Fourier transform, less weighting of k^2 emphasizes the bonds between a central metal atom and a light back-scatterer such as oxygen and carbon. The k^2-weighted Fourier-transformed spectra in Fig.S4 (ESI†) firmly support the enhanced structural ordering for the D800 and D825 samples. Additionally, the effect of the Sn treatment for one step-annealed α-Fe_2O_3 fabricated at 800 °C is investigated. In Fig.4c, the position of the Fe−O peak does not change, but its intensity decreases upon the addition of Sn. The peak position does not change, even after a 10-fold increase in the molar Sn concentration. This suggests that, since FTO is sufficiently deformed at an annealing temperature of 800 °C, the subsequent surface Sn^{4+} treatment does not alter the α-Fe_2O_3 lattice significantly (due to relatively short annealing time of 13.5 min). An excess amount of Sn is no longer doped into the hematite material, and it may remain in the form of a tin oxide layer (SnO_x). Recalling the results in Fig.4a, FTO has no influence on α-Fe_2O_3 upon annealing at 550 °C; thus, the Sn surface treatment is so effective that it can alter the Fe−O bond distance in the α-Fe_2O_3. This may be due to the longer annealing time (4 h) in the case of the LT550-Sn10 sample.

Photoelectrochemical study

The effects of FTO deformation (caused by HT-annealing) and surface treatment by Sn^{4+} on the PEC performance and the onset potential behavior of hematite photoanodes in a 1 M NaOH electrolyte under 1 sun illumination were investigated. Fig.5a shows the current density–voltage (*J*–*V*) curves of pristine and Sn-doped α-Fe_2O_3 photoanodes annealed at low temperature. The onset potential (V_{onset}) was determined by measuring the potential at the intersection point of the dark current and the tangent at maximum slope of photocurrent.[42] The V_{onset} value as low as 0.7 V_{RHE} was observed for pristine LT550 hematite with photocurrent reaching to *ca.* 120 μA cm^{-2} at 1.23 V_{RHE}. The photocurrent plateau was attained to 160−170 μA cm^{-2} at 1.6 V_{RHE} toward the onset of the dark current. The surface treatment with 1 mM Sn^{4+} resulted in an anodic shift in the V_{onset} of Sn-doped α-Fe_2O_3 photoanode by a value of 80 mV and lead to a significant enhancement in the photocurrent (J_{ph}=160 μA cm^{-2} at 1.23 V_{RHE}), saturating to 250 μA cm^{-2} at 1.23 V_{RHE}. Upon further increase in Sn^{4+} concentration to 5 mM, the V_{onset} shifted slightly further toward more anodic region. Although, a higher photocurrent compared to the pristine and 1 mM Sn-doped α-Fe_2O_3 photoanodes (J_{ph}=185 μA cm^{-2} at 1.23 V_{RHE}) was recorded. With 10 mM Sn, the onset shifted to become more anodic with a decrease in J_{ph} at 1.23 V_{RHE}, but resulting in similar saturation photocurrent at dark current onset region. This suggests that with higher Sn^{4+} content, the water oxidation reaction at lower applied potentials in Sn-doped α-Fe_2O_3 is sluggish. The reason for the late onset potential can be ascribed to the unfavourable surface properties (which will be discussed later) that result in poor hole-transfer properties at the surface due to higher interfacial charge recombination. It should be noted that Sn^{4+} overlayer in excess (in the form of a SnO_x resistant layer) may block the transport of holes and decrease the PEC performance. Therefore, it is necessary to have the optimum concentration of Sn^{4+} ions on the surface without blocking the transfer of holes. Table 2 shows the V_{onset} values for all the photoanodes.

Fig.5b shows the *J*–*V* curves of pristine α-Fe_2O_3 photoanodes prepared at different annealing conditions. Among the HT-annealed samples, D800 shows cathodic shift in V_{onset} value (ca. 0.8 V). In addition, the STP800 photoanode (after second HT-annealing treatment) showed J_{ph} of 500 μA cm^{-2} at 1.23 V_{RHE}, which is a four-fold increase compared to the LT-annealed α-Fe_2O_3 photoanode. This improvement is mainly due to Sn enrichment from FTO deformation.

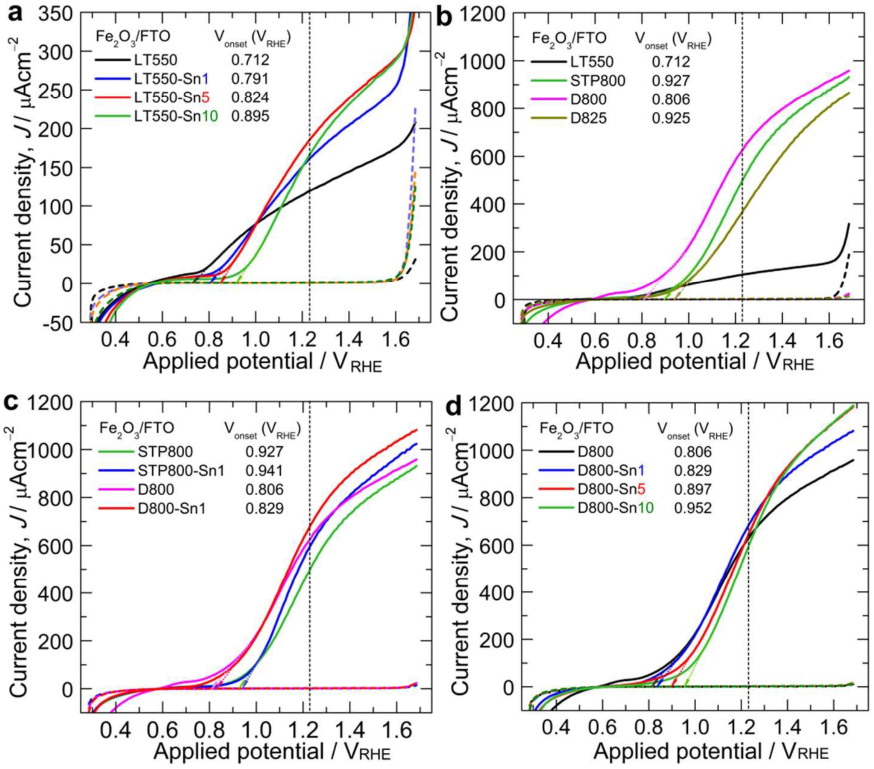

Fig. 5 Current density–voltage (*J*–*V*) curves of (a) pristine and Sn-doped α-Fe_2O_3 photoanodes fabricated by LT-annealing at 550 °C, (b) pristine α-Fe_2O_3 photoanodes fabricated with different annealing conditions, (c) pristine and 1 mM Sn-doped α-Fe_2O_3 photoanodes fabricated at high temperature by two-step and one-step annealing methods, and (d) pristine and Sn-doped α-Fe_2O_3 photoanodes fabricated by one-step HT-annealing at 800 °C. The tangent arrows pointing toward the X-axis gives the onset potential (V_{onset}) values of all the α-Fe_2O_3 photoanodes.

The photocurrent of the α-Fe_2O_3 photoanode was further improved to ~633 μA cm^{-2} at 1.23 V_{RHE} by one-step annealing condition. This superior performance is due to the optimum amount of Sn that was diffused into the hematite lattice from FTO deformation with a minimal loss in its conductivity. The V_{onset} of STP800 and D825 photoanodes shifted anodically by 80 and 120 mV, respectively, with reference to D800. The D825 also exhibited low photocurrent with no clear plateau region. The reason for such deleterious behavior is due to the higher degree of Sn diffusion doping (forming a resistant SnO_x layer) as well as severe FTO deformation that results in a greater loss of FTO conductivity.

Fig.5c shows the *J*–*V* curves of pristine and 1 mM Sn-doped α-Fe_2O_3 photoanodes prepared by two-step and one-step annealing methods. Almost no change in the onset potential was observed for Sn-doped α-Fe_2O_3 photoanodes irrespective of the methods; however, in both cases, the plateau region of the photocurrent increases almost linearly and is highest for the one-step annealed photoanode (~690 μA cm^{-2} at 1.23 V_{RHE}). This observation suggests that Sn^{4+} ions that are incorporated into the hematite lattice through the surface help to improve the charge transfer kinetics, thereby improving the photocurrent at applied. The sharp rise of photocurrents observed beyond the onset potential and the tendency of saturation in the high potential region (>1.0 V_{RHE}) indicate the improved charge transfer and collection efficiency of photoanodes upon incorporation of Sn^{4+} ions into the hematite lattice.[43] Since a greater improvement was observed for the Sn-doped α-Fe_2O_3 photoanodes prepared by the one-step method, the Sn^{4+} concentration was also varied to 5 and 10 mM in order to see the Sn effect of onset potential behavior as photocurrent.

Fig.5d shows the *J*–*V* curves of pristine and Sn-doped α-Fe_2O_3 photoanodes prepared by the one-step HT-annealing method for different Sn^{4+} concentrations. For 5 mM Sn^{4+}, the V_{onset} of Sn-doped α-Fe_2O_3 was displaced anodically by 130 mV and also resulting in a slight decrease in the photocurrent at 1.23 V_{RHE}.

UV-Vis spectroscopy

Light absorption studies of semiconducting materials can provide important insight into their interaction with photon energies and help determine methods to modulate the solar energy conversion. Fig.S5a (ESI†) shows the UV-Vis absorbance (the measure of the absorbed photons) of pristine and Sn-doped α-Fe_2O_3 photoanodes prepared by LT-annealing. The absorbance is increased slightly at higher wavelengths with a slight decrease in the band gap energy (~2.0 from 2.1 eV) due to Sn incorporation. The behavior of light absorption for Sn-doped hematite samples is generally similar to that of undoped hematite but quite different within the visible spectral range between 400 and 600 nm. The influence of Sn doping on the light absorption properties of hematite is reported to be dependent on the fabrication temperature. Jang *et al*. reported a slight decrease in the light absorption of 4% Sn-doped hematite.[44] Alternatively, a remarkable increase in the light absorption of Sn-doped hematite fabricated at high annealing temperatures (> 600°C), where atomic Sn is diffused from FTO deformation, has been observed.[5, 45] The band gap narrowing could be due to changes in the lattice parameters that were caused by doping,[46] which is reflected in the synchrotron XRD and XAFS studies.

Fig.S5b (ESI†) shows absorbance plots of pristine α-Fe_2O_3 photoanodes prepared at different annealing conditions. The light absorbance in LT-annealed and one-step annealed hematite samples is higher in the higher wavelength region, with a noticeable decrease in the band gap energy, and is lower for one-step annealed hematite. However, the fraction of light absorption in two-step-annealed hematite is lower due to the reflective nature of the film. Fig.S5c (ESI†) shows the absorbance of pristine and 1 mM Sn-doped α-Fe_2O_3 photoanodes fabricated at high temperature by two-step and one-step annealing methods. The light absorption properties of the photoanodes appear to be different. Although 1 mM Sn doping did not alter the band energy, the light absorbance was increased considerably. The difference is very small at the absorption edge but quite obvious in the high energy region. This spectral behavior follows the same trend as that of the *J*–*V* characteristics of the hematite photoanodes (as studied earlier). The increased absorbance in the one-step annealed hematite could be due to its higher content of diffused Sn^{4+} ions.

Fig.S5d (ESI†) shows the absorbance of pristine and Sn-doped α-Fe_2O_3 photoanodes prepared at high temperature by the one-step annealing method. With further surface addition of Sn^{4+} ions, the light absorption is slightly increased. This could be due to excess Sn^{4+} ions migrated from the surface into the hematite lattice, altering the surface and optical properties. Thus, Sn doping affects the structural, opto-electronic, and surface state properties of hematite in a more predictable way, which eventually determines the water splitting performance of the photoanodes.

Electrochemical impedance spectroscopy (EIS)

The charge transfer processes, which dictate the photocurrent response, that occur across the electrolyte and the surface of the electrode were investigated using EIS. Fig. 6a shows Nyquist plots (real *vs*. imaginary impedance) of pristine and Sn-doped α-Fe_2O_3 photoanodes prepared by LT-annealing. The results obtained from EIS were fitted using circuit elements consisting of one resistor and two RC circuits in parallel.[15] Table 2 depicts the EIS parameters obtained by fitting the Nyquist plots with equivalent circuits for the pristine and Sn-doped Fe_2O_3 films fabricated with different annealing temperatures and methods. The series resistance (R_s) is comprised of the resistances from FTO and the external wiring contacts. Since the resistance of the external contacts is unchanged, and because this value is small compared to that of the FTO resistance, the latter can be considered to be the main contributor to R_s. The value of R_s for all of LT-annealed hematite photoanodes is similar, suggesting that no deformation occurred in the FTO. However, the diameter of the semicircles related to the charge transfer resistance (R_{ct}) decreased monotonically as the Sn^{4+} concentration was increased from 0 to 10 mM. This suggests that Sn aids in the efficient charge transfer of photogenerated charge carriers. The surface state capacitance (C_{ss}) is the capacitance representing the charge stored in the surface states. The trap resistance (R_{trap}) accounts for the transfer of charges between the surface-trap state and the bulk semiconductor. The Css and Rtrap values, meant for trapping holes (to advance the water oxidation reaction), decrease as the Sn concentration increases. The higher the trap state capacitance (C_{ss}), the greater the number of trap states that are filled in the hematite film, resulting in an increased carrier density. This result clearly explains the decrease in the onset potential that was observed in the *J*–*V* curve of the LT-annealed photoanodes.

Fig.6b shows Nyquist plots of pristine α-Fe_2O_3 photoanodes prepared at different annealing conditions. The LT-annealed pristine α-Fe_2O_3 photoanode showed a higher R_{ct}, as can be seen from the increased semicircle diameter. The R_{trap} value is higher because of low electronic conductivity since Sn is not doped into the hematite at low temperatures. The R_s is low (17.77 Ω) because FTO undergoes no severe change in its conductivity during LT-annealing. During two-step annealing, the value of R_s is increased (84.57 Ω) and the value of R_{ct} is decreased. This is mainly due to the fact that HT-annealing causes the diffusion of Sn^{4+} ions into the hematite lattice from FTO deformation, improving the electronic conductivity. The one-step annealing further decreased both the Rs and Rct values due to the slight increase in the Sn content from FTO with a minimal loss in the conductivity. The value of C_{ss} for D800 is higher than that for the STP800 photoanode, indicating that more holes can be accumulated in the intermediate trap states, thereby facilitating the participation of holes in the photocurrent conversion processes. The lower R_{ct} and R_{trap} values further indicate an increased number of charge carriers in the film, which facilitate the charge transfer of holes to the donor species in solution and suppress the recombination of photogenerated electron–hole pairs to improve the photocurrent.[47] However, with a further increase in the one-step annealing temperature (to 825 °C), severe deformation in FTO occurs, leading to a greater loss in conductivity. This is reflected in the Nyquist plot by the higher R_s value.

To support these findings, the Nyquist plots of FTO electrodes were fabricated independently at the corresponding annealing conditions, as shown in Fig.S6 (ESI†). The figure shows how the conductivity of FTO changes as a result of the different annealing conditions. FTO deformation does not occur in the LT-annealed sample, as indicated by the unchanged Rs value for bare and annealed FTO. The loss in FTO conductivity is minimal for one-step-annealed FTO

Table 2 The EIS and Mott-Schottky parameters obtained by fitting equivalent circuits for the Nyquist plots of pristine and Sn-doped Fe_2O_3 films fabricated by different annealing temperatures and methods.

Samples/	R_s	R_{trap}	C_{bulk}	$R_{ct,trap}$	C_{ss}	$R_{s\,[FTO]}{}^{a}$	V_{onset}	V_{fb}	N_D
Parameters	Ω cm^2	Ω cm^2	$C_{[CPE]}$ / μF	Ω cm^2	$C_{[CPE]}$ / μF	Ω cm^2	V *vs* RHE	V *vs* RHE	cm^{-3}
Bare FTO	--	--	--	--	--	10.77	--	--	--
LT550	17.77	468.80	1.07	3433	11.765	16.64	0.712	0.756	0.370×10^{19}
LT550-Sn1	18.20	12.13	4.66	2212	5.811	--	0.791	0.723	0.488×10^{19}
LT550-Sn5	18.17	83.83	8.75	1804	0.246	--	0.824	0.744	0.375×10^{19}
LT550-Sn10	17.62	7.29	17.41	1821	0.032	--	0.895	0.723	0.509×10^{19}
STP800	84.57	107.90	69.48	445	5.971	65.26	0.927	0.262	4.725×10^{19}
STP800-Sn1	46.10	85.13	95.94	191	2.061	--	0.941	0.223	8.178×10^{19}
D800	70.16	23.60	10.89	425	14.268	41.18	0.806	0.381	6.479×10^{19}
D800-Sn1	63.66	24.78	20.85	309	8.254	--	0.829	0.373	6.967×10^{19}
D800-Sn5	66.86	31.31	40.03	248	5.805	--	0.897	0.517	9.791×10^{19}
D800-Sn10	68.50	36.39	187.27	288	4.885	--	0.952	0.556	11.594×10^{19}
D825	221.80	156.90	35.69	239	1.902	115.32	0.925	0.102	7.867×10^{19}

[a] $R_{s[FTO]}$ represents the series resistance obtained for bare and annealed FTO substrates prepared with identical annealing environments (similar to those of Fe_2O_3/FTO samples).

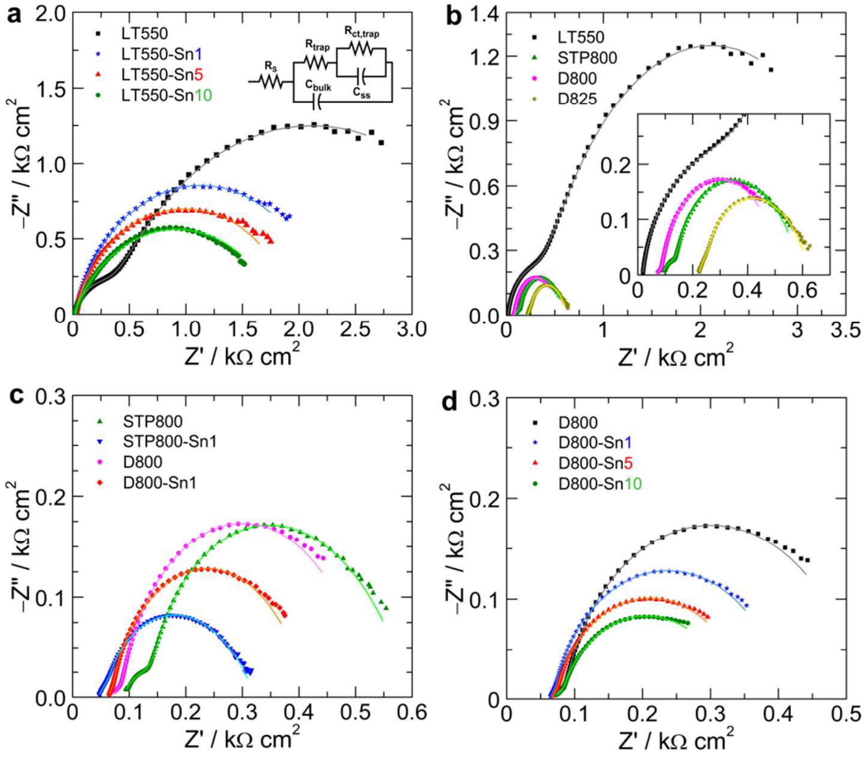

Fig. 6 Nyquist plots (real *vs.* imaginary impedance) of (a) pristine and Sn-doped α-Fe_2O_3 photoanodes fabricated by LT-annealing at 550 °C, (b) pristine α-Fe_2O_3 photoanodes fabricated at different annealing conditions, (c) pristine and 1mM Sn-doped α-Fe_2O_3 photoanodes fabricated at high temperature by two-step and one-step annealing methods, and (d) pristine and Sn-doped α-Fe_2O_3 photoanodes fabricated by one-step HT-annealing at 800 °C. EIS data were obtained at a bias potential of 1.23 V_{RHE} under 1 sun illumination in 1 M NaOH. The discrete symbols and the solid lines/curves in the plots represent the experimental data and the results of fitting, respectively. The inset of figure 6a shows the equivalent electrochemical circuit used for fitting all the Nyquist plots.

because the R_s value is relatively small compared to that of the two-step annealed sample. Severe FTO deformation can be seen in one-step annealed FTO at 825 °C for 13.5 min. The EIS study of FTOs is concurrent with hematite films prepared on FTO at the corresponding annealing conditions. In order to determine the optimum Sn content that should be diffused into hematite, a comparative study of the two-step and one-step annealed hematite with 1 mM Sn was performed. Although the C_{ss} value is higher for D800, the Rtrap value is much lower than that for the LT550 sample. Hence, a relatively lower onset potential for LT550, compared to D800, can be seen. Among the HT-annealed samples, D800 showed the highest C_{ss} value, which is a possible explanation for its lower onset potential.

Fig.6c shows Nyquist plots of the pristine and Sn-doped α-Fe_2O_3 photoanodes prepared by the two-step and one-step methods. The addition of 1 mM Sn^{4+} improved the R_{ct} value in both the two-step and one-step annealed Sn-doped α-Fe_2O_3 photoanodes. However, despite of the relatively low J_{ph} value at 1.23 V_{RHE}, the R_{ct} value is lowest for the 1 mM Sn-doped α-Fe_2O_3 photoanode prepared by the two-step annealing method. This could be due to the higher slope of the J_{ph} curve because a steep increase in photocurrent is typical of low recombination rates. However, the interfacial extraction of photogenerated holes from the hematite surface toward the electrolyte for water oxidation (oxygen evolution) is lower because of the concomitant loss of photogenerated holes. This is caused by the fact that the number of surface states is lower, as indicated by the decrease in the C_{ss} and R_{trap} values. In other words, appropriate amount of surface states helps to increase the yield of long-lived holes accumulating at the electrode surface. Fig.6d shows the Nyquist plots of pristine and Sn-doped α-Fe_2O_3 photoanodes prepared by the HT-annealing method. Both the R_s and R_{ct} values were decreased for 1 mM Sn^{4+}, which is consistent with the increments in the photocurrent. However, the R_{ct} values are still lower for 5 and 10 mM Sn^{4+}, despite the slight decrease in J_{ph}. Thus, a slightly higher photocurrent in Sn-doped hematite is caused by the increased donor density due to Sn diffusion doping, which drives the separation of charge carriers at higher applied potentials.

Mott–Schottky study

Values of charge carrier concentration (donor density, N_D), in pristine and Sn-doped α-Fe_2O_3 photoanodes were estimated via Mott–Schottky analysis.[48] The plots were measured at an AC frequency of 0.5 kHz and an AC amplitude of 10 mV under dark conditions in 1 M NaOH electrolyte. The positive slopes of the plots of the inverse-square of space charge capacitance (C_s) versus the applied potential for pristine and Sn-doped α-Fe_2O_3 photoanodes indicate that the photoanodes were all n-type semiconductors. A lower slope in the plots implies a higher N_D value. Fig.7a shows Mott–Schottky plots of pristine and Sn-doped α-Fe_2O_3 photoanodes prepared by LT-annealing. The higher slope of the LT550 sample accounts for its low donor density because no Sn ions are diffused at low temperature. The flat band potential (V_{fb}) is an important characteristic of semiconductor as it reflects the position of its Fermi level before contact with the electrolyte.

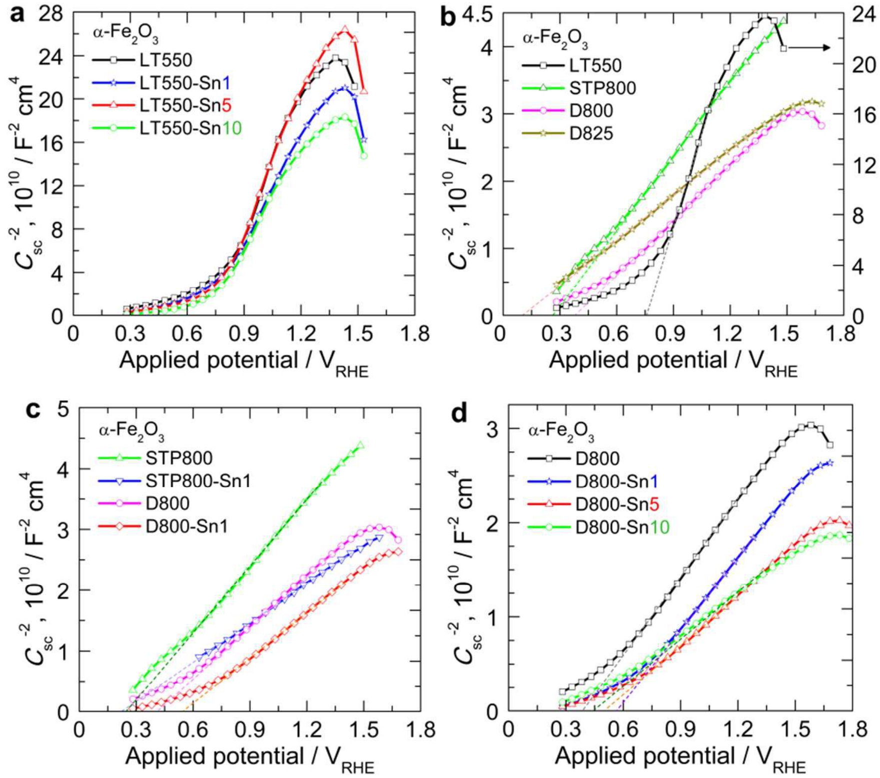

Fig. 7 Mott–Schottky plots of (a) pristine and Sn-doped α-Fe_2O_3 photoanodes fabricated by LT-annealing at 550 °C, (b) pristine α-Fe_2O_3 photoanodes fabricated at different annealing conditions, (c) pristine and 1 mM Sn-doped α-Fe_2O_3 photoanodes fabricated at high temperature by two-step and one-step annealing methods, and (d) pristine and Sn-doped α-Fe_2O_3 photoanodes fabricated by one-step HT-annealing at 800 °C.

No significant changes in the V_{fb} values were observed, although the N_D value was slightly increased when the Sn concentration increased from 0.370 × 10^{19} (for pristine photoanodes) to 0.509 × 10^{19} cm^{-3} (for 10 mM Sn-doped α-Fe_2O_3 photoanode). This observation suggests that Sn was not appreciably doped into the LT-annealed α-Fe_2O_3 photoanodes. Instead, it most likely segregated onto the surface or within the hematite in the form a thin SnO_2 layer, which acts as an efficient electron transmitter.

Fig.7b shows the Mott–Schottky plots of pristine α-Fe_2O_3 photoanodes prepared at different annealing conditions. The slope of the Mott–Schottky plot was lowest for the D825 sample, which means that a higher amount of Sn diffused into the hematite lattice as a result of FTO deformation. This results in a higher N_D value (7.867 × 10^{19} cm^{-3}). The N_D value for the one-step annealed α-Fe_2O_3 photoanode was 6.479 × 10^{19} cm^{-3}, which is higher than that of the two-step annealed α-Fe_2O_3 photoanode. However, the incorporation of 1 mM Sn^{4+} via surface treatment resulted in a significant increase in the N_D value (8.178 × 10^{19} cm^{-3}) for the two-step annealed α-Fe_2O_3 as compared to that of the one-step annealed α-Fe_2O_3 photoanode. This increase in donor density is reflected in the *J*–*V* measurement of the STP800-Sn1 sample, which displays a higher photocurrent at a higher potential with a higher slope. This suggests that the electron-hole separation rate is faster at relatively higher applied potential. The V_{fb} values (Table 2) for the LT550, STP800, D800, and D825 photoanodes were 0.712, 0.262, 0.381, and 0.102 V_{RHE}, respectively. Relatively, lower observed V_{fb} value for LT550 sample could be attributed to the reduced grain boundaries. Recently, prolonged low-temperature annealing (350 °C) by controlling the oxidation time was reportedly suppressed the grain boundaries, which down-shifted the V_{fb} as well as lowered the V_{onset} of α-Fe_2O_3 films.[49]

Fig.7c shows the Mott–Schottky plots of pristine and Sn-doped α-Fe_2O_3 photoanodes prepared by two-step and one-step methods. The one-step-annealed pristine and Sn-doped α-Fe_2O_3 photoanodes showed higher donor densities as compared to the two-step annealed photoanodes; this is expected due to their higher amount of externally-incorporated Sn. Fig.7d shows the Mott–Schottky plots of pristine and Sn-doped α-Fe_2O_3 photoanodes prepared by HT-annealing. Amongst the HT-annealed α-Fe_2O_3 photoanodes, the N_D value increased from 6.479 × 10^{19} cm^{-3} for the pristine photoanode to 11.594 × 10^{19} cm^{-3} for the 10 mM Sn-doped α-Fe_2O_3 photoanode. The V_{fb} values for the LT550, STP800, D800, and D825 photoanodes were 0.381, 0.373, 0.517, and 0.556 V_{RHE}, respectively. Consistent N_D values on the order of 10^{18}–10^{19} cm^{-3} have been reported for un-doped hematite nano-structured electrodes.[48, 50, 51]

In general, V_{fb} has a good correlation with the V_{onset} of anodic photocurrents, and gives information as to how much the actual electrolytic potential can be saved in a given electrochemical reaction. In most cases, the position of the conduction band nearly coincides with that of the flat band potential. If the conduction band of a photoanode is energetically higher than the hydrogen evolution potential, the photogenerated electrons can flow to the counter electrode and reduce protons resulting in hydrogen gas evolution without external applied voltage. With a photoanode having more negative (cathodic) onset potential, a more efficient PEC cell can be constructed. This shift of the V_{fb} is due to unpinning of the energy bands. This effect can be caused by trapping of photogenerated minority carriers in the surface states or by a very low rate of minority-carrier transfer.[52, 53] As the holes accumulate at the surface, an additional capacitance can occur in a limited potential range due to the surface states, which can be seen in Table 2 with higher value of Css for LT-annealed samples. The V_{fb} and N_D can give information about the width of space charge layer (W_{SCL}) as a function of applied potential and can be determined using relation (3):[54]

$$W_{\mathrm{SCL}} = \sqrt{\frac{2\varepsilon\varepsilon_0(V-V_{\mathrm{fb}})}{eN_{\mathrm{D}}}} \qquad (3)$$

It is noteworthy that the charge separation is only effective for electron-hole pairs that are generated sufficiently close to the interface. i.e. electron-hole pairs that are generated within the space charge later are readily separated by migration within the electrical field (band bending). But, pairs that are generated close enough to the SCL can also be separated, provided that the diffusion of electrons is faster than the competing recombination of electron-hole pairs. Therefore one would ideally look for a SCL as large as possible. Apparently, the W_{SCL} is larger for LT550 sample owing to lower N_D as well as higher V_{fb} values. The R_s value for LT550 sample is low because loss of conductivity is very minimal as Sn is not leached from FTO at low temperature. These are the reasons that collectively facilitate efficient separation of charge carriers and hence onset potential is earlier for LT550. On the other hand, in the case of HT-annealed samples, Sn is doped into the hematite from FTO that causes increase in N_D and hence improve the photocurrent response at higher potentials. Now that N_D values are higher and V_{fb} is relatively lower than the LT550 samples, the W_{SCL} values for HT-annealed samples would be lower (according to equation 3). Therefore, the separation of electron-hole pairs is not at faster pace for lower applied potentials.

The level of Sn doping must be optimized such that the structural ordering in hematite is maintained. In this scenario, it is important to consider the effect of Sn doping on the formation of defect states in hematite. Surface states are reported to initiate water oxidation, even without illumination, during electron transfer that involves tunnelling across the space-charge region.[36] The behavior of the onset potential can be explained by considering the intensities of the (104) can be explained by considering the intensities of the (104) and (110) hematite planes, as discussed in the XRD study.

Fig.8 shows the schematic of the charge transfer mechanism and reveals the role of the crystalline orientations of hematite photoanodes that are affected upon Sn^{4+} doping

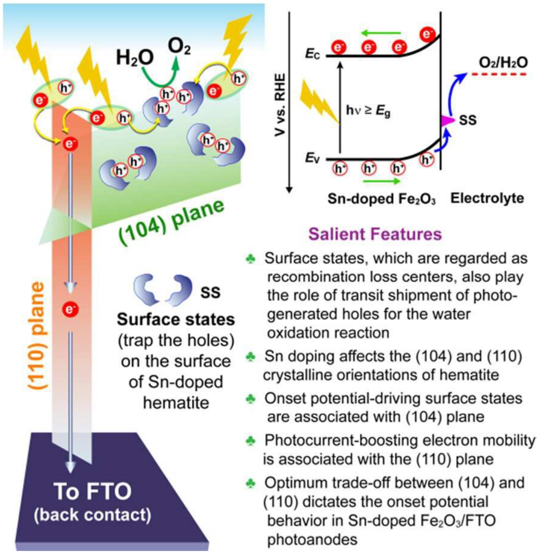

Salient Features

- Surface states, which are regarded as recombination loss centers, also play the role of transit shipment of photo-generated holes for the water oxidation reaction
- Sn doping affects the (104) and (110) crystalline orientations of hematite
- Onset potential-driving surface states are associated with (104) plane
- Photocurrent-boosting electron mobility is associated with the (110) plane
- Optimum trade-off between (104) and (110) dictates the onset potential behavior in Sn-doped Fe_2O_3/FTO photoanodes

Fig. 8 Schematic showing the role of surface trap states and the electronic conductivity associated with the (104) and (110) crystalline orientations of hematite, respectively.

under different annealing circumstances. Under illumination, numerous photo-induced electron-hole (e^--h+) pairs are generated. The surface states associated with the (104) plane trap the photogenerated holes at the hematite surface and make these holes available in the vicinity of electrolyte for water oxidation reactions. Alternatively, the photogenerated electrons follow the high mobility path associated with the (110) plane, thereby increasing the photocurrent of hematite. The LT550 photoanode, which possessed a more cathodic onset potential in comparison to LT550-Sn10, exhibited an intense (104) peak. This means that the surface states associated with this plane take part in speeding up the water oxidation reaction. In contrast, the intensity of the (104) plane is decreased after Sn^{4+} treatment and the intensity of the (110) plane is also very close to that of (104). This suggests that the electron mobility is also relatively high, which leads to a higher photocurrent. The photocurrent increment is related to the higher orientation along the (110) plane; this is likely caused by the favourable conductivity of the majority carriers (electrons) along the [110] axis (c-axis), which is perpendicular to the FTO substrate. In the case of STP800 samples, the (104) site that speeds up the water oxidation reaction is lower than that for D800. This is the reason for the anodic shift in the onset potential of the photocurrent. In the case of Sn-doped D800 samples, the (104) peak intensity was slightly lower, but the difference between the (104) and (110) planes continues to increase. The decreasing contribution of the (110) sites not only decreases the electron mobility but also impedes the tunnelling of charge carriers. This explains why there is no significant photocurrent enhancement in Sn-doped α-Fe_2O_3 photoanodes fabricated by HT-annealing. This observation suggests that an optimum trade-off between the (104) and (110) sites is of paramount importance for lowering the onset potential and enhancing the photocurrent to drive the water oxidation reaction.

Conclusions

In summary, we have successfully demonstrated as to how Sn^{4+} doping under different annealing circumstances affects the electronic conductivity and surface defect states, which eventually dictates the water oxidation photocurrent and the onset potential of hematite (α-Fe_2O_3) photoanodes fabricated by PRED. The importance of surface states in mediating the hole transfer mechanism to control the onset potential is probed and validated with the help of powerful electrochemical impedance spectroscopy (EIS) analysis and synchrotron XRD studies. Incorporation of Sn^{4+} into α-Fe_2O_3 was achieved by means of either external (surface treatment)- or self (underlying FTO substrate)-doping. Low (550 °C)- and high (800 °C)-temperature annealing treatments were chosen for external Sn doping to fabricate Sn-doped α-Fe_2O_3/FTO photoanodes. At low temperature, the Sn^{4+} doping enriched the conductivity of α-Fe_2O_3/FTO and improved the photocurrent response. However, this shifted the onset potential anodically, which was ascribed to the hematite surface states (as seen from the decrease in the surface state capacitance in EIS). At high temperature, the FTO conductivity and the hematite surface properties were altered due to excess incorporation of Sn ions (SnO_x) into the hematite matrix, which also resulted in an anodic shift of the onset potential. The use of different annealing conditions, which causes the lattice distortion and deformation-directed Sn diffusion-doping, was also found to affect the hematite surface states and the onset potential. One-step annealing at 800 °C resulted in a sufficient number of favourable surface states, which initiated the water oxidation reaction earlier by trapping a maximum number of photogenerated holes; this led to a cathodic shift in the onset potential. It was shown that Sn doping affects the crystalline orientations that are linked with the formation of surface defect states in hematite. The XRD study is consistent with the EIS analysis and revealed that the (104) plane, which is responsible for the surface states, is more prevalent in the one-step annealed sample compared to the two-step annealed hematite. Moreover, the differences between the (104) planes and the conducting (110) planes were minimal for the one-step annealed hematite. Thus, it was concluded that the onset potential behavior and water oxidation reaction of Sn-doped α-Fe_2O_3 photoanodes depend collectively on the substrate conductivity, surface states, donor density, and the optimum balance between the (104) and (110) facet sites.

Acknowledgements

This research was supported by the Basic Science Research Programs of the National Research Foundation of Korea (NRF, 2012R1A6A3A04038530), as well as Korea Ministry of Environment (MOE) as Public Technology Program based on Environmental Policy. The authors also acknowledge the Basic Research Project (GP2015-007, 15-3224) of the Korea Institute of Geoscience and Mineral Resources (KIGAM) funded by the Ministry of Science, ICT and Future Planning of Korea.

Note and References

1. A. B. Murphy, P. R. F. Barnes, L. K. Randeniya, I. C. Plumb, I. E. Grey, M. D. Horne and J. A. Glasscock, *Int. J. Hydrogen Energy*, 2006, **31**, 1999−2017.
2. P. S. Shinde, A. Annamalai, J. H. Kim, S. H. Choi, J. S. Lee and J. S. Jang, *Sol. Energy Mater. Sol. Cells*, 2015, **141**, 71−79.
3. C. D. Bohn, A. K. Agrawal, E. C. Walter, M. D. Vaudin, A. A. Herzing, P. M. Haney, A. A. Talin and V. A. Szalai, *J. Phys. Chem. C*, 2012, **116**, 15290−15296.
4. Y. Ling, G. Wang, D. A. Wheeler, J. Z. Zhang and Y. Li, *Nano Lett.*, 2011, **11**, 2119−2125.
5. R. Morrish, M. Rahman, J. MacElroy and C. A. Wolden, *ChemSusChem*, 2011, **4**, 474−479.
6. L. Xi, S. Y. Chiam, W. F. Mak, P. D. Tran, J. Barber, S. C. J. Loo and L. H. Wong, *Chem. Sci.*, 2013, **4**, 164−169.
7. R. L. Spray, K. J. McDonald and K.-S. Choi, *J. Phys. Chem. C*, 2011, **115**, 3497−3506.
8. F. Le Formal, N. Tetreault, M. Cornuz, T. Moehl, M. Gratzel and K. Sivula, *Chem. Sci.*, 2011, **2**, 737−743.
9. F. Le Formal, K. Sivula and M. Grätzel, *J. Phys. Chem. C*, 2012, **116**, 26707−26720.
10. L. Wang, C.-Y. Lee, A. Mazare, K. Lee, J. Müller, E. Spiecker and P. Schmuki, *Chem. – Eur. J.*, 2014, **20**, 77−82.
11. Z. Fu, T. Jiang, L. Zhang, B. Liu, D. Wang, L. Wang and T. Xie, *J. Mater. Chem. A*, 2014, **2**, 13705−13712.
12. X. Li, P. S. Bassi, P. P. Boix, Y. Fang and L. H. Wong, *ACS Appl. Mater. Interfaces*, 2015, **7**, 16960−16966.
13. L. Xi, P. S. Bassi, S. Y. Chiam, W. F. Mak, P. D. Tran, J. Barber, J. S. Chye Loo and L. H. Wong, *Nanoscale*, 2012, **4**, 4430−4433.
14. M. Zhang, W. Luo, N. Zhang, Z. Li, T. Yu and Z. Zou, *Electrochem. Commun.*, 2012, **23**, 41−43.
15. B. Klahr, S. Gimenez, F. Fabregat-Santiago, T. Hamann and J. Bisquert, *J. Am. Chem. Soc.*, 2012, **134**, 4294−4302.
16. O. Zandi and T. W. Hamann, *Phys. Chem. Chem. Phys.*, 2015, **17**, 22485−22503.
17. M. P. Dare-Edwards, J. B. Goodenough, A. Hamnett and P. R. Trevellick, *J. Chem. Soc., Faraday Trans. 1*, 1983, **79**, 2027−2041.
18. N. Guijarro, M. S. Prevot and K. Sivula, *Phys. Chem. Chem. Phys.*, 2015, **17**, 15655−15674.
19. T. Hisatomi, F. Le Formal, M. Cornuz, J. Brillet, N. Tétreault, K. Sivula and M. Grätzel, *Energy Environ. Sci.*, 2011, **4**, 2512−2515.
20. X. Yang, R. Liu, C. Du, P. Dai, Z. Zheng and D. Wang, *ACS Appl. Mater. Interfaces*, 2014, **6**, 12005−12011.
21. F. Le Formal, M. Graetzel and K. Sivula, *Adv. Funct. Mater.*, 2010, **20**, 1099−1107.
22. S. M. Wilhelm, K. S. Yun, L. W. Ballenger and N. Hackerman, *J. Electrochem. Soc.*, 1979, **126**, 419-424.
23. J. Leduc and S. M. Ahmed, *J. Phys. Chem.*, 1988, **92**, 6661−6665.
24. G. Horowitz, *J. Electroanal. Chem.*, 1983, **159**, 421−436.
25. V. M. Aroutiounian, V. M. Arakelyan, G. E. Shahnazaryan, G. M. Stepanyan, J. A. Turner and S. S. Kocha, *Electrochim. Acta*, 2000, **45**, 1999−2005.
26. H. K. Dunn, J. M. Feckl, A. Muller, D. Fattakhova-Rohlfing, S. G. Morehead, J. Roos, L. M. Peter, C. Scheu and T. Bein, *Phys. Chem. Chem. Phys.*, 2014, **16**, 24610−24620.
27. P. S. Shinde, A. Annamalai, J. Y. Kim, S. H. Choi, J. S. Lee and J. S. Jang, *J. Phys. Chem. C*, 2015, **119**, 5281−5292.
28. B. Ravel and M. Newville, *J. Synchrotron Radiat.*, 2005, **12**, 537−541.
29. J. J. Rehr, J. J. Kas, F. D. Vila, M. P. Prange and K. Jorissen, *Phys. Chem. Chem. Phys.*, 2010, **12**, 5503−5513.
30. R. L. Blake, R. E. Hessevic, T. Zoltai and L. W. Finger, *Am. Mineral.*, 1966, **51**, 123−129.
31. P. S. Shinde, A. Annamalai, J. H. Kim, S. H. Choi, J. S. Lee and J. S. Jang, *Data in Brief*, 2015, **5**, 796−804.
32. S. Hernandez, D. Hidalgo, A. Sacco, A. Chiodoni, A. Lamberti, V. Cauda, E. Tresso and G. Saracco, *Phys. Chem. Chem. Phys.*, 2015, **17**, 7775−7786.
33. J. Bisquert, in *Nanostructured Energy Devices: Equilibrium Concepts and Kinetics*, CRC Press, Boca Raton, FL, 2014, vol. 91, ch. 9, p. 275−320.
34. I. Cesar, K. Sivula, A. Kay, R. Zboril and M. Grätzel, *J. Phys. Chem. C*, 2009, **113**, 772−782.
35. K. Sivula, *J. Phys. Chem. Lett.*, 2013, **4**, 1624-1633.
36. L. M. Peter and K. G. Upul Wijayantha, *ChemPhysChem*, 2014, **15**, 1983-1995.
37. G. Rollmann, A. Rohrbach, P. Entel and J. Hafner, *Phys. Rev. B*, 2004, **69**, 165107/165101−165112.
38. J. Baltrusaitis, D. M. Cwiertny and V. H. Grassian, *Phys. Chem. Chem. Phys.*, 2007, **9**, 5542−5554.
39. T. Yamashita and P. Hayes, *Appl. Surf. Sci.*, 2008, **254**, 2441−2449.
40. A. Grosvenor, B. Kobe and N. McIntyre, *Surf. Sci.*, 2004, **572**, 217−227.
41. S. Gota, E. Guiot, M. Henriot and M. Gautier-Soyer, *Phys. Rev. B*, 1999, **60**, 14387−14395.
42. D. Cao, W. Luo, J. Feng, X. Zhao, Z. Li and Z. Zou, *Energy Environ. Sci.*, 2014, **7**, 752−759.
43. A. G. Tamirat, W.-N. Su, A. A. Dubale, H.-M. Chen and B.-J. Hwang, *J. Mater. Chem. A*, 2015, **3**, 5949−5961.
44. J. S. Jang, J. Lee, H. Ye, F.-R. F. Fan and A. J. Bard, *J. Phys. Chem. C*, 2009, **113**, 6719−6724.
45. K. Sivula, R. Zboril, F. Le Formal, R. Robert, A. Weidenkaff, J. Tucek, J. Frydrych and M. Gratzel, *J. Am. Chem. Soc.*, 2010, **132**, 7436−7444.
46. J. D. Bryan and D. R. Gamelin, in *Prog. Inorg. Chem.*, John Wiley & Sons, Inc., 2005, DOI: 10.1002/0471725560.ch2, p. 47−126.
47. C. Miao, T. Shi, G. Xu, S. Ji and C. Ye, *ACS Appl. Mater. Interfaces*, 2013, **5**, 1310−1316.
48. A. A. Tahir, K. U. Wijayantha, S. Saremi-Yarahmadi, M. Mazhar and V. McKee, *Chem. Mater.*, 2009, **21**, 3763−3772.
49. B. Iandolo, H. Zhang, B. Wickman, I. Zoric, G. Conibeer and A. Hellman, *RSC Adv.*, 2015, **5**, 61021−61030.
50. J. Y. Kim, G. Magesh, D. H. Youn, J.-W. Jang, J. Kubota, K. Domen and J. S. Lee, *Sci. Rep.*, 2013, **3**, 2681−2688.
51. J. A. Glasscock, P. R. Barnes, I. C. Plumb and N. Savvides, *J. Phys. Chem. C*, 2007, **111**, 16477−16488.
52. A. McEvoy, M. Etman and M. Hemming, *J. Electroanal. Chem. Interfac. Electrochem.*, 1985, **190**, 225−241.
53. H.-M. Kühne and H. Tributsch, *J. Electroanal. Chem. Interfac.Electrochem.*, 1986, **201**, 263−282.
54. J. Kelly and D. Vanmaekelbergh, *Electrochimica acta*, 1998, **43**, 2773−2780.